nature communications

Article

https://doi.org/10.1038/s41467-025-64644-z

Design of direction-independent hydrovoltaic electricity generator based on all-foam asymmetric electrode

Received: 19 June 2024

Accepted: 18 September 2025

Yaohao Zhang[1,2], Fei Yu[1,2], Liying Wang[1,2], Xijia Yang[1,2], Yue Yang[1,2], Xuesong Li[1,2] ✉, Yang Gao[1,2], Yi Jiang[3], Ke Jiang[4], Wei Lü[1,2,4] ✉, Xiaojuan Sun[4] ✉ & Dabing Li[4] ✉

To obtain higher open-circuit voltage, metal sheets and carbon electrodes are often used to construct asymmetric electrodes of water evaporation generators. However, the metal sheets hinder water evaporation, limiting device performance. Herein, an all foam-structured asymmetric water evaporation generator independent of water evaporation direction is designed. ZIF-67 has been shown to effectively enhance the surface potential of foamed iron electrodes and provide Co^{2+} charge carriers for charge transfer. After combining the FI-based cathode with melamine foam and a composite carbon cloth anode to form the FI/ZIF67@CMF-MF-CC@CNTs type device, compared with the metal sheet electrode, the current density is increased by 300% up to 862 μA/cm^2 and the voltage is increased by 50% up to 782 mV. The optimal power density is 101 μW/cm^2. We also demonstrate present device in both energy harvesting and daily electronics, highlighting its potential for scalable energy utility.

In recent years, a clean power generation method, relying on the interaction between water molecules and solid surfaces, has attracted widespread attention, and referred as the hydrovoltaic electricity generators (HEGs)[1–5]. HEGs can be categorised into planar, sandwich, and asymmetric types based on their device structure.[6–10] With the development and combination of different electrode materials, it has been found that the choice of anode and cathode materials directly affects the open-circuit voltage of the device, with the device voltage increasing as the surface potential difference between the electrodes rises.[11–13] By combining easily processed carbon electrodes (such as carbon black,[14,15] graphene oxide,[16,17] etc.) with metal electrodes, asymmetric HEGs are formed, creating a high potential difference between the electrodes and enabling high voltage output. Additionally, the rate of water evaporation is a key factor influencing current density, the higher the evaporation rate, the greater the current density.[18–20] By directly adopting porous electrodes (carbon cloth[21,22], carbonized wood[23,24]) or pre-treating the electrodes, water molecules can be stabilized to evaporate, thereby obtaining stable current[25,26]. Therefore, enhancing the output power of HEGs can be achieved by increasing the potential difference between the two electrodes and promoting water evaporation.

Metal-organic frameworks (MOFs) possess high surface potential and specific surface area[27], which can enhance the surface potential of materials and promote moisture evaporation[28,29]. This suggests that they hold promise for increasing open-circuit voltage and short-circuit current in the production of HEGs. For instance, coating MOF-801 onto carbon nanotubes (CNTs) creates nanoscale water channels, achieving an open-circuit voltage of ~2.2 V and a short-circuit current of 1.9 μA[30]. Additionally, a layered orientation Cu (BDC-OH) MOF assembly, prepared using hydrolysis, anion exchange reactions, and heteroepitaxial

---

[1]Key Laboratory of Advanced Structural Materials, Ministry of Education and School of Materials Science and Engineering, Changchun University of Technology, Changchun, China. [2]Advanced Institute of Materials Science, Changchun University of Technology, Changchun, People's Republic of China. [3]School of Science, Changchun Institute of Technology, Changchun, China. [4]State Key Laboratory of Luminescence Science and Technology, Changchun Institute of Optics, Fine Mechanics and Physics, Chinese Academy of Sciences, Changchun, People's Republic of China. ✉e-mail: lixuesong@ccut.edu.cn; lw771119@hotmail.com; sunxj@ciomp.ac.cn; lidb@ciomp.ac.cn

growth, can realise an open-circuit voltage of ~0.6 V and an output power of 1.56 nW/cm[2,20]. However, the aforementioned studies only create nanoscale water channels, neglecting the interactions between the MOFs and the electrodes. Moreover, research on electrodes has previously focused on carbon electrodes that are easy to process and modify[31–34], lacking exploration of optimisation strategies for other electrode types[35–37]. While metal electrodes can form high-output HEGs with carbon electrodes without any processing, dense metal sheets may restrict water evaporation[38–40], resulting in only transient electrical signals when used as top electrodes[41,42]. The limited applications of MOFs and electrode optimisation approaches significantly hinder the further development and subsequent commercialisation of HEGs.

To address the aforementioned issues, this work presents a design for a fully foam asymmetric HEGs that is independent of the direction of water evaporation. The cathode uses foamed iron (FI) as the main metal electrode, preventing water molecules from evaporating only from one side of the HEG. The FI electrode is reinforced with the Co^{2+} metal-organic framework (ZIF-67), a material with a stable preparation method[43–45]. On one hand, it can enhance the surface potential to increase the voltage; on the other hand, it provides Co^{2+} as charge carriers, improving the current density. First-principles calculations and finite element simulations show that the addition of ZIF-67 effectively enhances the interaction between H_2O and the electrode, providing a foundation for the improvement of current-voltage performance. The anode employs a CNTs-modified carbon cloth (CC) electrode (CC@CNTs), and the two electrodes are separated by melamine foam (MF). The structure is stacked to form a FI/ZIF67@CMF-MF-CC@CNTs type HEG unit. HEGs composed of FI/ZIF67@CMF exhibit an open-circuit voltage of ~0.782 V and a current density of 862 μA/cm² at room temperature, increasing by ~50% and ~300%, respectively, compared to iron sheet electrodes. The device achieves optimal output power of 101 μW/cm² at a 999.9 Ω load. Additionally, the device is flexible, easily bent to form wearable devices such as rings or bracelets, providing power for devices like LEDs and watches, showcasing its potential in wearable device applications. It also demonstrates high integration stability; both voltage and current increase linearly, and the generated power can be easily stored using capacitors or batteries, potentially leading to its development into self-powered supercapacitors or batteries.

Results

Preparation and properties of HEGs

The schematic diagram shown in Fig. 1a illustrates the HEG device, while the actual device and energy spectrum analysis are presented in Fig. S1 (SI). The carbon electrode (CC@CNTs) and the composite foam iron electrode (FI/ZIF67@CMF) are separated by a 0.5 mm MF, resulting in the asymmetric structure designated as FI/ZIF67@CMF-MF-CC@CNTs. The surface area of the carbon electrode is significantly increased after acidification and coating with CNTs, where the acidified CNTs wrap around the CC surface (Fig. S2, SI), effectively increasing the number of oxygen-containing groups on the CC surface, transforming the treated CC into a hydrophilic material (Fig. S3, SI). MF is employed as an isolation layer between the two electrodes (Fig. S4, SI). The porous structure of MF can store several times its own mass of water (Fig. S5, SI), thus extending the stable operating time of HEGs.

The preparation method of FI/ZIF67@CMF is illustrated in Fig. S6 (SI), where FI is initially acidified and passivated to enhance its specific surface area and form a dense oxide film to prevent oxidation[46,47]. Through X-ray photoelectron spectroscopy (XPS) tests (Fig. S7, SI), the FI surface after strong acid passivation treatment simultaneously formed Fe(II) and Fe(III). Combined with X-ray diffraction (XRD) analysis (Fig. S8, SI), it can be confirmed that the passivated surface of FI forms a dense Fe_3O_4 layer. Subsequently, ZIF-67-deposited CMF is pressed onto the FI surface at 10 MPa for 1 min to form the FI/ZIF67@CMF composite electrode. The N_2 adsorption-desorption isotherms are shown in Fig. S9 (SI). The BET surface area and total pore volume of the composite FI are 1.7378 m²/g and 0.010295 cm³/g respectively. Fig. 1b depicts the schematic diagram of the FI composite electrode, where ZIF-67@CMF does not completely fill all the pores of FI but forms a unilateral filling. Under pressure, ZIF-67@CMF fractures and embeds into the gaps of FI (Fig. 1d–f), further increasing the specific surface area of the FI composite electrode, enhancing the effective area for interaction with water molecules. Firstly, we conducted Raman and Fourier-transform infrared analysis (FTIR) on the surface (Fig. 1g, h), confirming that the MF underwent sufficient carbonisation and that the attachment of ZIF-67 provided additional nitrogen and oxygen functional groups to the electrode surface. XPS characterisation of the FI composite electrode surface (Fig. S10, SI) revealed a significant presence of N-O bonds, C-O bonds, and oxygen functional groups (-OH), effectively promoting interaction between the electrode and H_2O, thereby enhancing the device's current density. Additionally, XRD characterisation of the FI composite electrode surface (Fig. 1i) indicated that a passivation layer of Fe_3O_4 formed on the treated FI surface, achieving stable connection with ZIF-67@CMF[48].

After thoroughly wetting the electrode by dripping water, the different components of the FI/ZIF67@CMF composite electrode are assembled with the CC@CNTs to form the HEG device, and its output electrical signal is tested (Fig. 1c). The current density of the HEG using only carbon materials is only 141 nA/cm² and 328 nA/cm² (Fig. S11, SI), much lower than that of the HEG with FI as the cathode. However, by applying pressure to form a composite electrode, the water channels on the surface of FI are further enhanced (Fig. S12, SI), increasing the interaction area between H_2O and the electrode, which improves the HEG current density. Further addition of ZIF-67, on the one hand, reduced the surface Zeta potential of FI (Fig. S13a, SI) and compensated for the decrease in the FI electrode potential caused by passivation (Fig. S13b, SI), thereby increasing the potential difference between the asymmetric electrodes and further improving the open-circuit voltage[49,50]. On the other hand, the Co^{2+} in ZIF-67 can act as charge carriers between the electrodes, boosting the HEG current density. Compared to the FI-MF-CC@CNTs HEG, the current density of the FI/ZIF67@CMF-MF-CC@CNTs HEG increases from 206 μA/cm² to 832 μA/cm², and the open-circuit voltage rises from 0.5 V to 0.78 V. The current density increased by 300%, and the open-circuit voltage increased by 50%.

Finite element analysis and first-principles calculations

Fig. 2a–c) illustrates the surface charge densities of FI, ZIF-67, and FI/ZIF-67. With reference to the scale in the figure, it can be observed that in the presence of FI alone, the electron distribution on the Fe surface is uniform due to its metallic nature, resulting in a relatively low surface charge density and an overall neutral charge. In contrast, ZIF-67 exhibits characteristics of a metal-organic framework, where the surface charge is related to its elemental composition. Oxygen atoms display a slight negative charge, while carbon atoms show a slight positive charge; however, the overall structure remains electrically neutral. When ZIF-67 comes into contact with FI, a significant charge transfer occurs, with electrons from the FI surface transferring towards the oxygen, leading to a distinctly positive charge on the Fe surface and a notable negative charge on the oxygen surface. Given that the other electrode is CC@CNTs, the higher negative potential will facilitate the generation of higher voltages in the HEGs. Additionally, the increased reactivity of the oxygen atoms enhances the likelihood of forming hydrogen bonds with H_2O, thereby promoting interactions between the electrodes and H_2O. A similar scenario occurs on the CMF surface (Fig. S14, SI), where deposition of ZIF-67 leads to further electron transfer and hybridization of surface charges, resulting in an elevated potential on the ZIF-67@CMF surface. However, the electron activity

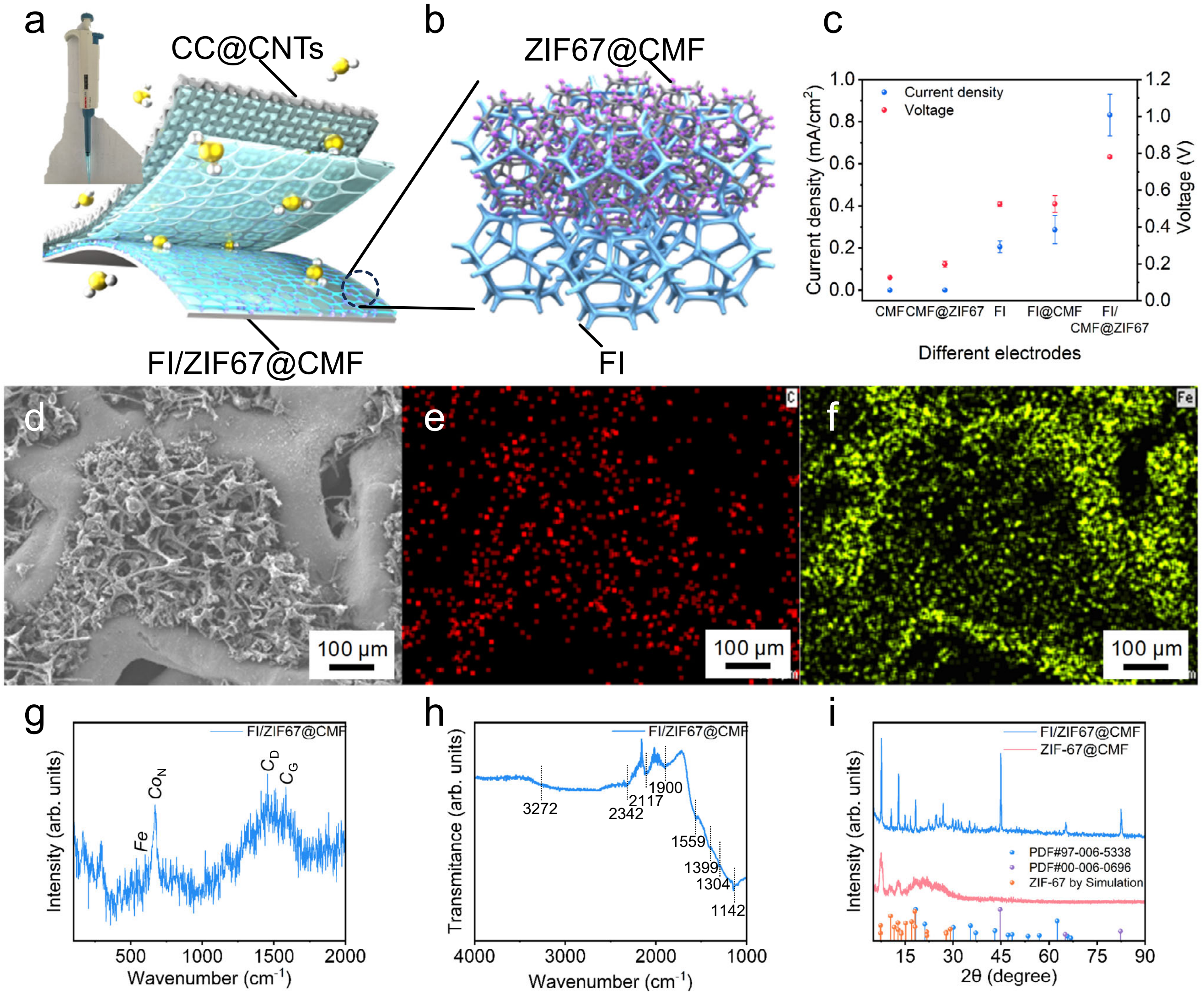

Fig. 1 | The schematic diagram, performance, and surface characterization of the hydrovoltaic electricity generator (HEG) device. a Schematic diagram illustrating the HEG device. The illustration in the figure is a digital photograph of a pipette, used to represent the need to wet the HEG with a drop of water before use. **b** Schematic representation of the FI/ZIF67@CMF electrode structure. **c** The average current density (blue) and voltage (red) of the electrodes with different components and CC@CNTs-based HEG under conditions of 20 °C and 20% RH for 30 min. The error bars represent the standard deviation. **d** scanning electron microscopy (SEM) image and energy dispersive spectroscopy (EDS) analysis of FI/ZIF67@CMF, with carbon element (**e**) depicted in red and iron element (**f**) in green. Similar structures were observed in all 20 samples from different batches. **g** Raman spectrum of FI/ZIF67@CMF and (**h**) Fourier-transform infrared spectroscopy analysis. **i** X-ray diffraction (XRD) curves of FI/ZIF67@CMF (blue) and ZIF67@CMF (red). The X-ray source was Cu K alpha, and the XRD spectrum simulation of ZIF-67 was performed using "Reflex" in Materials Studio 2020. Source data are provided as a Source Data file.

on the C surface is much lower than on the FI surface, resulting in a less significant increase, consequently leading to less pronounced voltage enhancement in the resulting HEGs. From (Fig. 2d–f), it can be observed that the combination of FI and ZIF-67 leads to hybridization of internal d and f orbitals, resulting in changes in the FI electrode surface potential. Before the combination, Fe atoms have lower charge density, and electrons in each orbital are in a relatively low state, while ZIF-67, despite having higher charge density, cannot effectively transfer electrons without a collector. After the combination, FI acts as a superior collector, and the composite of FI and ZIF-67 improves the overall surface potential, forming a composite electrode with both high surface potential and excellent electron conduction ability. As a transition metal, Fe has highly active d and s orbital electrons. After hybridization with the s and d orbital electrons of elements such as C and O in ZIF-67, it is further strengthened, effectively increasing the potential difference between the two electrodes, thus resulting in a higher open-circuit voltage.

Fig. 2g and Fig. 2h illustrate the electrostatic field distribution between the FI composite electrode and the carbon electrode under wet and dry conditions, respectively. The polar water molecules transform the initially uniform electric field into a wavy pattern. As the polar water molecules move between the electrodes, the electrostatic field undergoes continuous fluctuations, generating an electrical signal. At the same time, under the influence of the electrostatic field, ions such as Co^{2+}, H_3O^+, and OH^- in the water undergo directional movement, which can also produce an electrical signal in the external circuit. Through the combined action of both factors, the HEG is able to generate a continuous electrical signal.

The process of interaction between water and the electrodes can be broken down into three steps (Fig. 3a). Step 1, When the electrodes are not in contact with H_2O, there is a stable potential difference between the electrodes, but without the help of charge carriers, no current can be detected in the external circuit. Step 2, when water comes into contact with both electrodes, it interacts with the electrode

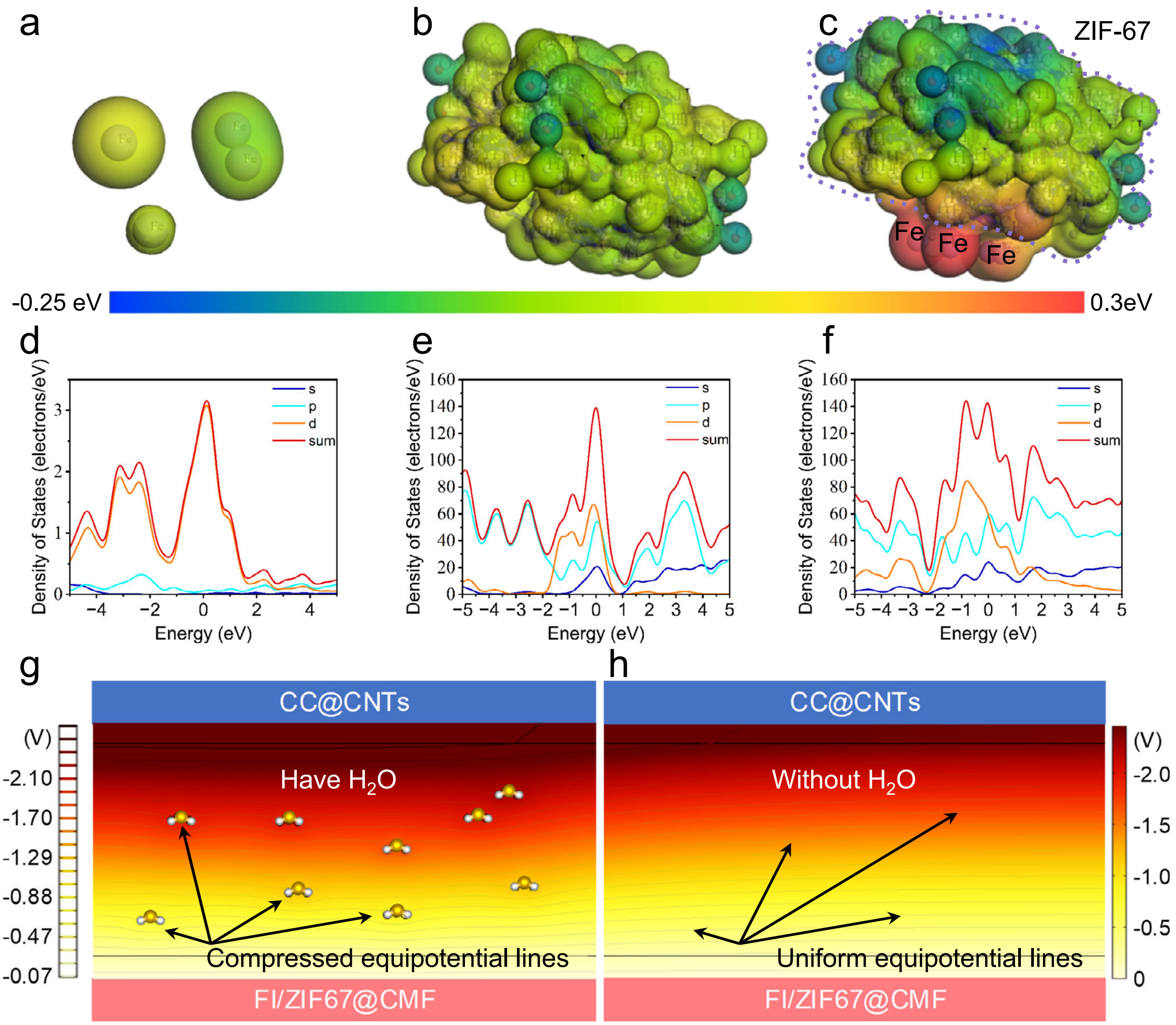

Fig. 2 | Surface electron and electrostatic field simulation. Depicts the surface charge density of (**a**) FI, (**b**) ZIF-67, and (**c**) FI/ZIF67, with the purple dashed lines in (**c**) representing ZIF-67 molecules. The differential charge density of (**d**) FI, (**e**) ZIF-67, and (**f**) FI/ZIF67 is also presented. Additionally, the electrostatic potential distribution between the two electrodes is shown in (**g**) with water molecules and (**h**) without water molecules. Source data are provided as a Source Data file.

surface, causing electron transfer on the electrode surface and forming a double layer (Fig. S15, SI). At the same time, the relevant ions in the electrodes undergo hydrolysis, generating charge carriers. Step 3, water moves between the electrodes through processes like evaporation. The hydrogen bonds of the water molecules drive the charge carriers to move between the electrodes. In conjunction with the schematic diagram of the two-dimensional charge carriers (electrons and ions) movement (Fig. S16, SI), after deionized water is dropped onto the HEG device, the hydrolysis-generated Co^{2+}, H_3O^+, and OH^- ions will form ionic charge carriers that move within the HEG. Under the potential difference between the electrodes, positively charged ions move towards the CC@CNTs electrode, while negatively charged ions move towards the FI/ZIF67@CMF electrode. As the ions migrate within the internal circuit, FI/ZIF67@CMF releases electrons in the external circuit and moves towards the CC@CNTs electrode, thereby completing the charge circuit formed by the ion migration within the internal circuit.

To further increase the surface area of the FI, acidification-passivation treatment was performed on the FI before preparing the composite electrode. The treated FI surface no longer exhibits a smooth curvature but rather shows numerous nanochannels for water (Fig. S17a, SI), combined with further analysis by energy dispersive spectroscopy (EDS) revealing a uniform oxide film (Fig. S17b-c, SI). An increased number of nano- to sub-nano-sized water channels can effectively enhance the interaction area between H_2O and the electrodes. Additionally, under capillary action, water molecules can move more quickly across the electrode surface, facilitating evaporation and thereby increasing the current density of HEGs. To quantify the movement of H_2O within the water channels on the electrode surface, we employed a relationship between the grayscale in SEM images and the surface morphology of the materials. Using binary colour coding, we identified the water channels (Fig. S18a, SI) and conducted finite element analysis of the microscale water flow based on the Stokes flow equation. Fig. 3b presents the simulated results of water flow on the FI surface based on Stokes flow approximation[51,52]. According to the computational fitting results, the water flow velocity in narrow regions is several times higher than that in wide regions. If it were a metal sheet, it could be considered as having an infinitely wide surface on the microscale, where water molecules would remain stationary after being affected by gravity, rather than undergoing further movement

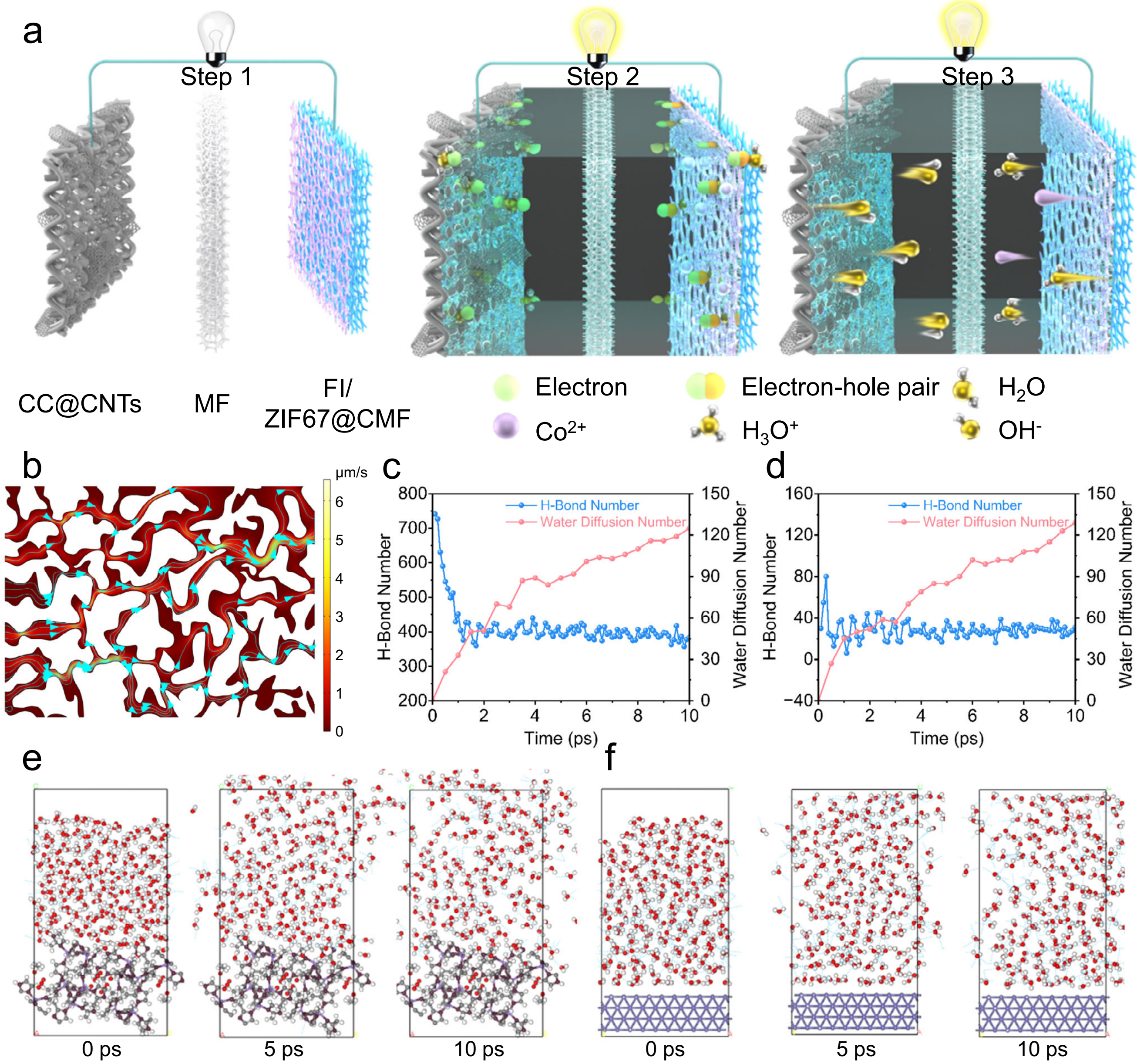

Fig. 3 | Reaction mechanism and interface analysis. a Schematic diagram illustrating the water evaporation power generation mechanism. **b** model of the movement of water molecules within microscale crevices based on Stokes flow. The changes in the number of hydrogen bonds (blue) and the number of water molecule diffusions (red) on the (**c**) ZIF-67 surface and (**d**) Fe surface within 10 ps. The distribution of water molecules on the (**e**) ZIF-67 surface and (**f**) Fe surface within 10 ps. The red spheres represent oxygen (O) atoms, the white spheres represent hydrogen (H) atoms, the purple spheres represent cobalt (Co) atoms, the brown spheres represent nitrogen (N) atoms, and the blue spheres represent iron (Fe) atoms. The blue dashed line represents the hydrogen bond. Source data are provided as a Source Data file.

under the influence of surface tension, as on the FI surface. This implies that the rate of interaction between FI and water molecules is much higher than that with metal sheets. Furthermore, based on the Brinkman assumption satisfying the Stokes equation, an analysis of the model was conducted (Fig. S18b, SI), where the inlet and outlet positions of the water flow were exchanged under the assumption of incompressible water flow. Comparing the results with Stokes flow revealed similar pressure or velocity curves, further confirming that the microstructure effectively promotes the movement of water molecules. This also explains why the current density of the foam iron is much higher than that of metal sheets, not only because the surface area of the foam iron is higher than that of iron sheets but also because the rate of water molecule movement on the electrode surface is faster[53,54].

ZIF-67 not only enhances the electrode surface potential but also increases the interaction frequency between water molecules and the electrode. To simulate the device's performance after sufficient wetting, water molecules are placed in clusters on the material's surface, directly mimicking the evaporation process. Fig. 3e, f illustrate the movement of water molecules on the ZIF-67 (111) and Fe (111) surfaces over different time intervals. Comparatively, the interaction between ZIF-67 and water molecules is significantly more intense than that with Fe. The oxygen and nitrogen-containing groups on the ZIF-67 surface can form hydrogen bonds with water molecules, while Fe struggles to do so. Additionally, as a MOF material, ZIF-67 has pores that allow water molecules to penetrate deeper and interact with internal oxygen-containing groups, thereby promoting increased current density. In contrast, Fe, being a dense metallic crystal, restricts water

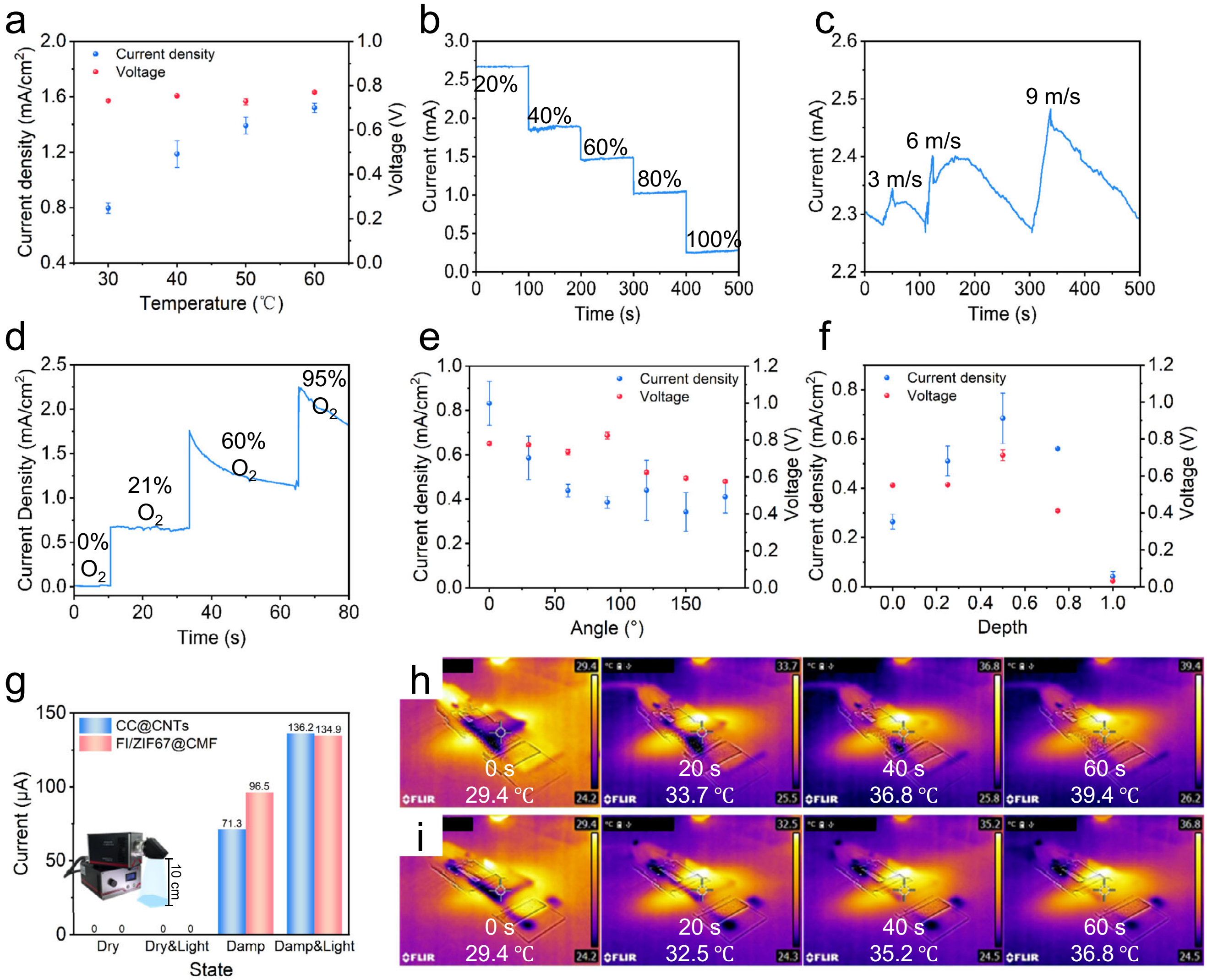

Fig. 4 | The impact of the environment on the power generation of hydrovoltaic electricity generator (HEG) devices. a Current densities (blue) and voltages (red) of HEGs at different temperatures for 30 min at RH = 20%. Current variation of HEGs at (**b**) different humidity, (**c**) different wind speed, (**d**) and different oxygen environment. The labels in the figure represent environmental humidity, wind speed, and oxygen content, respectively. Current densities (blue) and voltages (red) of HEGs with an effective area of 2 × 2 cm rotated at (**e**) different angles and (**f**) immersed in water at different ratios for 30 min. The error bars represent the standard deviation. **g** Current changes at CC@CNTs top electrode (blue) and FI/ZIF67@CMF top electrode (red) with different water contents (dry-wet) by irradiating the device surface with one sunlight intensity. Photothermal variations under wet conditions with (**h**) CC@CNTs and (**i**) FI/ZIF67@CMF as top electrodes, respectively. Source data are provided as a Source Data file.

molecules from entering and interacting with the material. Further comparisons of energy changes in both models over 10 ps (Fig. S19, SI) reveal that, starting from similar energy levels at 0 ps, the energy fluctuations in the ZIF-67 model are notably higher than in Fe, indicating a stronger interaction with H_2O. Moreover, we recorded the changes in the number of hydrogen bonds and the number of water molecules dissipating over 10 ps (Fig. 3c,d). The ZIF-67 model exhibits ten times the number of hydrogen bonds compared to the Fe model. In the ZIF-67 model, both H_2O-H_2O and H_2O-ZIF67 hydrogen bonds can form, whereas in the Fe model, only H_2O-H_2O bonds are present. Although the number of dissipated H_2O molecules is similar in both models over the same period, the greater variability in hydrogen bond numbers in the ZIF-67 model suggests that it can frequently form and break hydrogen bonds with H_2O. This direct interaction implies that ZIF-67 can enhance the energy collection during the water evaporation process, effectively increasing the device's current density. In summary, by combining ZIF-67 with Fe to form a composite electrode, both the surface potential of the electrode and the acquisition of evaporation energy are improved, resulting in a higher open-circuit voltage and increased short-circuit current for the device.

Environmental factors affecting HEGs

Since HEG generates electricity through the interaction between H_2O and the electrodes, environmental factors directly affect the strength of the electrical signal. A 2 × 2 cm HEG was fabricated as shown in Fig. S20 (SI), and environmental changes were controlled using a constant temperature and humidity system (Fig. S21, SI). At different temperatures, the current density of the HEG changes significantly. As the ambient temperature rises from 30 °C to 60 °C, the current density increases from 0.78 mA/cm^2 to 1.5 mA/cm^2, while the voltage remains relatively stable (Fig. 4a). This could be due to the higher evaporation rate of water with increasing temperature, leading to more frequent charge transfer between the water and the electrodes. On the other hand, the increased temperature may also intensify water hydrolysis, increasing the carrier concentration between the electrodes, resulting in a significant increase in current density. Meanwhile, as the temperature increases, although the Zeta potential and electrode potential of different electrode materials change to varying degrees, both the Zeta potential difference and electrode potential difference remain relatively stable compared to the changes in current (Fig. S22, SI). Therefore, the device voltage does not exhibit significant changes with temperature variation. When the ambient humidity is lower (Fig. 4b) and wind speed is higher (Fig. 4c), water evaporation intensifies, and the current density increases significantly, while the voltage remains relatively stable (Fig. S23, SI). This further confirms that the water evaporation rate is positively correlated with current density, but has no significant effect on voltage.

Fig. 4d shows the variation in current density of the HEG device under different O_2 concentrations. As shown in Fig. S24a (SI), to examine the power generation of the HEG device in an anaerobic environment, Ar was continuously pumped into the glove box. In the absence of O_2, the current density of the HEG device remained at ~10 μA/cm^2 due to the proton flow generated by the slow movement of H_2O in narrow channels and the changes in electron delocalization caused by evaporation (Fig. S24b, SI).[26,55] As the O_2 concentration increased, the current density gradually increased. When the O_2 concentration exceeded 95%, the current density even surpassed 2 mA/cm^2. Molecular dynamics simulations (Fig. S25a, SI) revealed that the presence of O_2 enhanced the interaction between H_2O and the electrode surface, significantly increasing the number of hydrogen bonds under the influence of O_2, thus promoting electron transfer between the electrode and H_2O. Additionally, differential charge density simulations (Fig. S25b, SI) showed that the electron activity at the Fe@H_2O@O_2 three-phase interface was significantly higher than that at the Fe@H_2O two-phase interface, further confirming that O_2 effectively enhanced the electrical signal.

Importantly, the use of the FI composite electrode addresses the issue of unidirectional evaporation in the device, effectively promoting the evaporation rate of water molecules. When FI/ZIF67@CMF and CC@CNTs are used, one acts as the bottom electrode and the other as the top electrode, without the concern that a dense electrode would block water evaporation and cause the HEG to stop working. As shown in Fig. S26a (SI), when HEG is rotated at different angles, it is considered to have the FI/ZIF67@CMF electrode as the top electrode when the angle exceeds 90°. During rotation, HEG consistently produces stable electrical signals (Fig. 4e). As the rotation angle increases, the binding force between the two electrodes decreases under the influence of gravity. Once the angle exceeds 90°, the binding force is improved, and the current density increases again. Furthermore, the effective evaporation area is a key factor affecting HEG's output current (Fig. 4f). When the HEG device is placed in a beaker and submerged to different depths (Fig. S26b, SI), if the HEG is fully exposed to air, it relies solely on the capillary action of MF to absorb water from the beaker. With too few water molecules between the two electrodes, the current density remains low. As the submersion depth increases, the current density gradually increases. However, after exceeding 50%, the effective evaporation area decreases, and the current density declines as well.

In the natural environment, both carbon and FI electrodes convert solar energy into heat energy, which promotes water evaporation[56–58]. One of the FI/ZIF67@CMF and CC@CNTs was used as the top electrode and the other as the bottom electrode, and the photo-thermal and power generation were examined under dry-humid conditions, respectively. Fig. 4g shows the current-voltage variations in different conditions. The inset in the figure shows the schematic diagram of the placement of the HEGs device, which is placed at a position of 10 cm away from the xenon lamp light source, so that the device can receive 1000 W/m^2 of light intensity steadily. Under dry conditions, after 60 s of illumination, the device with CC@CNTs as the top electrode reached a temperature of 84.5 °C (Fig. S27a, SI), whereas with FI/ZIF67@CMF as the top electrode, the temperature was only 62.2 °C due to metallic material reflection (Fig. S27b, SI). However, no current was observed either before or after illumination, and heating the device to 60 °C also failed to produce any current (Fig. S28, SI). Conversely, when the device was in a humid state, significant currents were generated regardless of whether FI/ZIF67@CMF or CC@CNTs were used as the top electrode, the device with FI/ZIF67@CMF as the top electrode outputs a current of 96.5 μA, while the device with CC@CNTs as the top electrode outputs a current of 56.3 μA. After 60 s of illumination, due to sunlight absorption and reflection by water, the temperature of the HEGs with CC@CNTs as the top electrode was 39.4 °C (Fig. 4h), while with FI/ZIF67@CMF as the top electrode, it was 36.8 °C (Fig. 4i), both lower than in dry conditions. However, short-circuit currents were significantly enhanced, reaching 135 μA in both cases. These experiments demonstrate that the current is not a photocurrent caused by light illumination, nor a thermoelectric current induced by heating. Instead, it is a current generated by water evaporation. Furthermore, water molecules can evaporate from any electrode (whether it be FI/ZIF67@CMF or CC@CNTs), and the resulting current is independent of the evaporation location, consistently producing stable current.

Scaling up and demonstration of HEGs

To verify the device's stability, HEGs were placed under ambient conditions (21 °C <T <25 °C, 20% <RH <25%) for long-term testing (Fig. 5a). Within 10 h, the output voltage reached up to 782 mV, with a current density of up to 862 μA/cm^2, demonstrating high stability and showing potential for practical applications. XRD testing was performed on the FI/ZIF67@CMF electrode after working for 10 h (Fig. S29, SI). The results were consistent with those before operation, and the decrease in the ZIF-67 peak intensity was caused by the hydrolysis of Co^{2+}. To confirm whether electrochemical corrosion occurs in the electrode material during use, the C-V curves of the HEG devices were tested at different scan rates. No oxidation-reduction peaks were observed in the discharge range (0-0.8 V) for all devices (Fig. 5b), confirming that no significant corrosion occurred in the electrodes during use. To further identify the potential negative voltage range where oxidation reactions might occur and to assess the stability of the device under acidic conditions, different HEG devices were tested in the range of -1.0 V to 1.0 V. The results show that the HEG device made with the original FI electrode, similar to the passivated FI/ZIF67@CMF composite electrode in pure water, did not exhibit any oxidation-reduction peaks (Fig. S30a,b, SI). However, in an acidic environment (pH=1), the original FI electrode generated distinct oxidation peaks, and as the test progressed, its surface morphology continuously changed, leading to further variations in the C-V curve (Fig. S30c, SI). In contrast, the HEG device made with the passivated FI/ZIF67@CMF composite electrode maintained a smooth C-V curve (Fig. S30d, SI), demonstrating that the composite electrode remains stable under different conditions. HEG integration can be easily achieved through series and parallel configurations. A small 1 × 1 cm unit of HEG was fabricated (Fig. S31, SI) and fixed to the front of a glass slide. By altering the circuit on the back of the glass slide, the conversion between series and parallel configurations can be achieved (Fig. S32, SI). As the number of parallel units increases (Fig. 5c), the HEG module's current rises from 0.65 mA to 3.6 mA, while the voltage of the HEG module increases from 0.71 V to 3.39 V as the number of series units increases (Fig. 5d). Fig. 5e shows the changes in current density, voltage, and power of HEG under different loads, with the power density reaching a peak value of 101 μW/cm^2 when the load is 999.9 Ω. Compared to other recent studies (Fig. 5f), the FI/ZIF67@CMF-MF-CC@CNTs-based HEG achieves a significant increase in power generation. A detailed comparison of materials, testing environments, and other factors can be found in Table S1,2 (SI).

To verify the general applicability of the optimized approach, other metal sheet electrodes (such as Cu, Ni, and Zn) were further

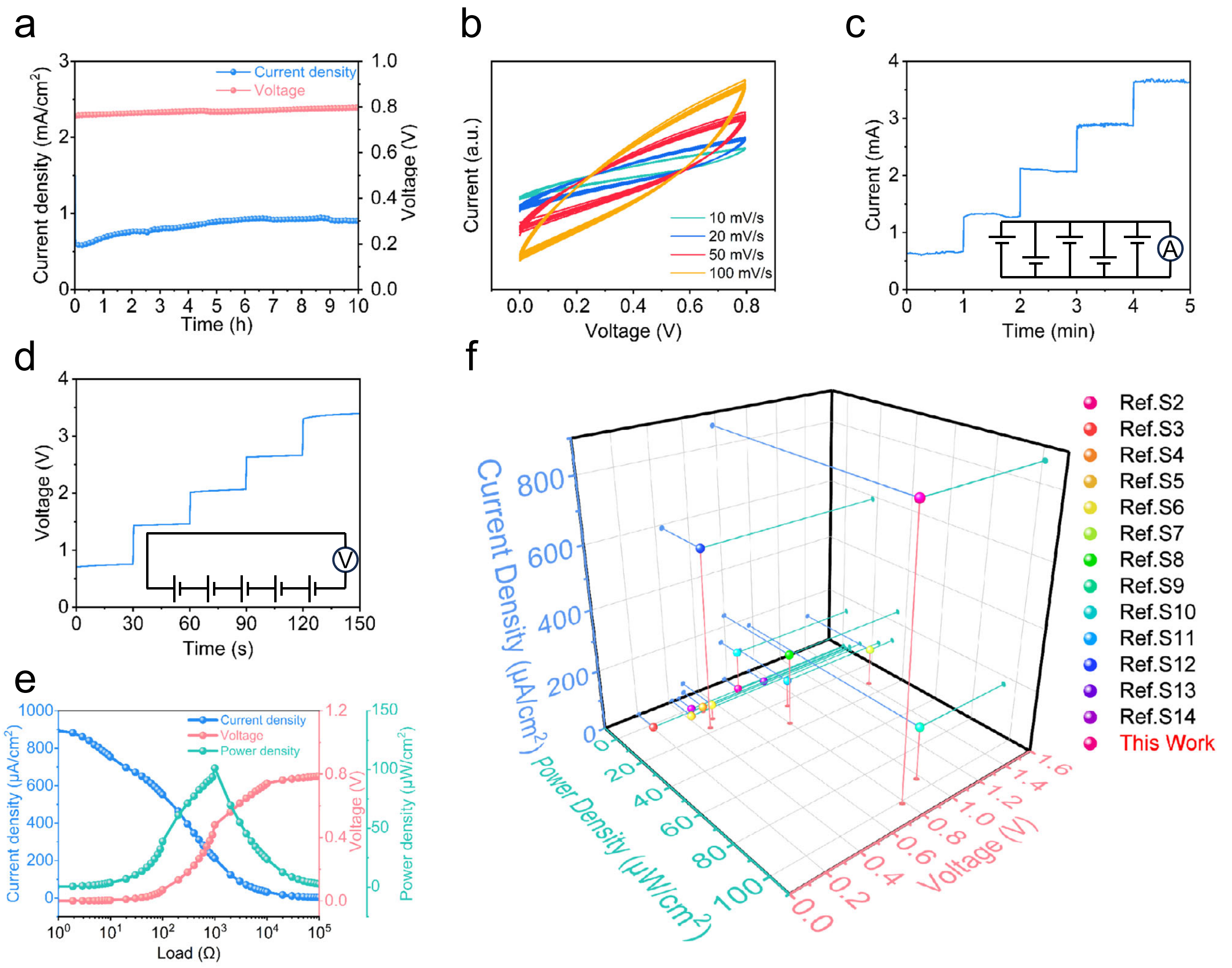

Fig. 5 | Stability and integration testing of hydrovoltaic electricity generator (HEG) devices. a Curves of HEGs open circuit voltage (red) and current density (blue) variations over 10 h under ambient conditions. **b** C-V curves of HEGs at different scan rates. (10 mV/s is green, 20 mV/s is blue, 50 mV/s is red, and 100 mV/s is orange) (**c**) Voltage variations of 5 serially connected HEGs 1× 1 cm unit devices. **d** Output current variations of 5 parallel-connected HEGs 1 × 1 cm units. The illustration shows a simplified circuit of the integrated HEG unit. **e** Variations in current density (blue), open circuit voltage (red), and power density (green) of HEGs under different loads. **f** Comparison of present work with other reports on HEGs devices. Source data are provided as a Source Data file.

optimized. By switching to metal foam and forming composites with ZIF-67, both the current density and voltage were improved to varying extents (Fig. 6a). Although these metals did not show as significant an improvement as FI, the current density increased by an average of 58.17%, and the voltage increased by an average of 25.00%, demonstrating the universality of the ZIF-67-enhanced metal electrode strategy (Fig. S33, SI). No obvious redox peaks were observed for the HEGs made of different metals at different scan rates (Fig. S34, SI). The distance between the electrodes and the tightness of the connection will directly affect the output current of the HEGs. In the previously mentioned water immersion and deflection experiments, the connectivity between the two electrodes of the HEGs was also reduced due to buoyancy or gravity, resulting in lower current density. To further investigate the effect of connection sealing on the power generation of HEGs, we utilised a 50 g weight as a pressure source for further exploration (Fig. S35, SI). The current density of the device varied with the placement and removal of the weight as shown in Fig. 6b. To prevent water molecules from blocking the diffusion for a long time due to the weights, they were placed on the surface of the device and then removed. When the weights were not placed, the current density stabilised at 0.75 mA. However, on placement, the current density increased significantly, rising to a staggering 2.4 mA, further confirming the effect of the connection on the output of the device. In the absence of pressure, some of the pores in the porous MF are occupied by air, hindering current conduction. However, applying pressure to the surface displaces the air with evaporated water molecules, ensuring continuous evaporation and replenishment of water molecules on the surface of the material, thereby increasing the current density. Furthermore, pressing the device does not have a significant impact on the output voltage (Fig S36, SI), with the voltage decreasing by only 3.9% after pressing. This further confirms that external factors are unlikely to affect the device's voltage. Fig. 6c shows the V-t curves of individual devices charging commercial capacitors of different capacities. As the capacitor capacity increases, the charging time also increases, but all achieve rapid charging within 3 s, demonstrating that the electrical energy generated by HEGs can be easily harvested. To further simulate the potential solution environments for HEGs in practical applications, we used various concentrations of NaCl solution to mimic sweat (0.03 M), physiological saline (0.9 M), and seawater (3.5 M), alongside samples of natural seawater. In a still indoor environment, we tested the current output of the HEGs. Fig. S37 (SI) shows the average voltage and current density over 30 min in different solutions. As NaCl concentration increased, there was no significant change in voltage, confirming that external environments

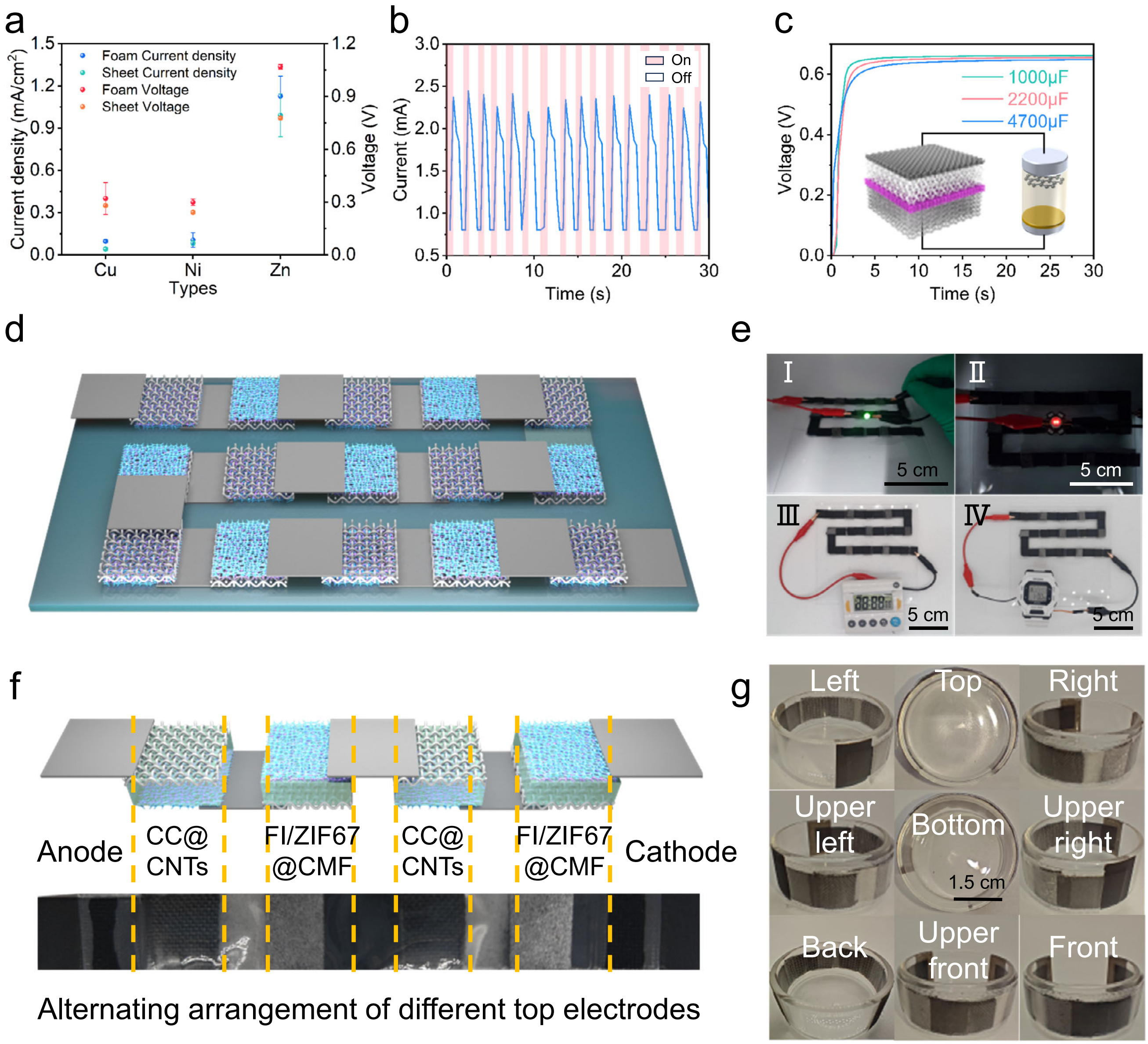

Fig. 6 | Integration and application of hydrovoltaic electricity generator (HEG) devices. a Current-voltage variations before and after optimization of different electrode materials (foam current density is blue, sheet current density is green, foam voltage is red, and sheet voltage is orange). **b** Detection of pressing signals. **c** Charging of individual HEGs for different capacity commercial capacitors (4700 μF is blue, 2200 μF is red, and 1000;μF is green). **d** Schematic diagram of the integrated assembly of 15 1 × 1 cm HEGs units in series. **e** I 4 series-connected units light up a green LED, II 5 series-connected units light up a large red LED, III 15 series-connected units drive a timer, IV 15 series-connected units drive an electronic wristwatch. The scale is 5 cm. **f** Schematic diagram and digital photo of four units composing the soft-packaged HEGs. **g** Digital photos of the soft-packaged HEGs taken from different angles after bending. The scale is 1.5 cm. The diameter of the Petri dish is 3 cm. Source data are provided as a Source Data file.

do not significantly impact voltage. However, current density increased with concentration, mainly due to the effective charge transfer between electrodes facilitated by hydrolysed Na^+ and Cl^-. Compared to natural seawater, the equivalent seawater exhibits a higher current density because the larger ions like Ca^{2+}, Mg^{2+}, and SO_4^{2-} in natural seawater hinder migration, affecting overall current density.

In order to achieve a high-power HEGs device, we integrated 15 HEGs units (1 × 1 cm) in series. As shown in Fig. 6d, for the purpose of circuit integration, the CC@CNTs and FI/ZIF67@CMF electrodes alternately serve as the top electrodes, with direct connections made using carbon tape. The voltage variation after the series connection is depicted in Fig. S38 (SI). Experimental results demonstrate that a series-integrated assembly of 4 units can light up a LED (Fig. 6e-I), while 5 series-integrated units can illuminate a large LED (Figure e-II). Furthermore, 15 series-connected units are capable of directly powering a timer (Figure e-III) or an electronic wristwatch (Figure e-IV). Supplementary Movie 1 presents a video of the 15-series integrated assembly powering an electronic wristwatch, showing good stability through repeated power-on and power-off tests. HEGs can convert low-grade thermal energy into electrical energy, absorbing the body's emitted heat and sweat. As shown in Fig. 6f, four HEGs units were prepared in a wearable format through soft packaging. To facilitate connection, the HEGs were alternately arranged, with FI composite electrodes and carbon electrodes serving as top electrodes, connected directly by conductive carbon tape, and finally thermally encapsulated with PET. To ensure stable water adsorption-evaporation, the PET was laser-engraved for perforation. The prepared soft-packaged HEGs can be shaped through bending, and Fig. 6g shows images of the bent soft-packaged HEGs from different angles, demonstrating stable power generation after bending. Fig. S39 (SI) shows the changes in current and voltage output of the device before and after bending. There is no significant variation in either current or voltage, demonstrating that the soft-pack HEGs maintain stable current output even after deformation. When further bent and worn on a finger, the soft-packaged HEGs can light up a yellow LED (Supplementary Movie 2). These experiments also prove the practical value of HEGs in flexible wearable energy.

Discussion

In summary, we have successfully developed a direction independent hydrovoltaic electricity generator based on all-foam asymmetric electrode. By addressing the unidirectional water evaporation, enhancing the electrode surface potential, and providing charge carriers, the current density and open-circuit voltage of the HEG device are simultaneously improved. Combining experimental research with theoretical calculations, we generate power through the electrostatic potential changes caused by water evaporation and the directional movement of charge carriers. Compared to metal foils, metal foam offers a higher specific surface area and better permeability, effectively promoting the interaction between water and the electrode, thereby increasing the current density. Additionally, the introduction of ZIF-67@CMF enhances the surface potential and charge carrier concentration of FI, leading to a simultaneous increase in both open-circuit voltage and short-circuit current of the HEG. The treated HEG exhibited a current density of 862 μA/cm^2 and an open-circuit voltage of 0.782 V, marking a 300% increase in current density and a 50% increase in open-circuit voltage compared to metal foil electrodes. The optimal output power reached 101 μW/cm^2, which can directly power wearable devices or be stored in commercial capacitors. By employing foamization and composite strategies, it can enhance the performance of various metal sheet electrodes, offering approaches for the fabrication and enhancement of HEGs electrodes.

Methods

Materials and reagents

Sulfuric acid (H_2SO_4, AR 98.08%), nitric acid (HNO_3, 65-68%), methanol (CH_3OH, AR 99.7%), ethyl alcohol (C_2H_6O, AR 99.7%), acetone (C_3H_6O, AR 99.5%) and cobalt nitrate hexahydrate ($Co(NO_3)_6{\cdot}6H_2O$, AR 98.5%) used in the experiment were purchased from China National Pharmaceutical Group Corporation. 2-methylimidazole ($C_4H_6N_2$) and NaCl (AR, 99.5%) was obtained from Aladdin. Carbon nanotubes (CNTs) and carbon cloth (CCs) were sourced from Taiwan Carbon Consortium. Melamine foam (MF), conductive carbon tape (CT), Carbon film, and Foamed iron (FI) were purchased from local markets. Unless otherwise specified, the H_2O resistance used in the experiment exceeded 18.2 MΩ·cm^{-1}. The natural seawater was collected from the Bohai Sea in China.

Preparation of ZIF-67 precursor

3 mmol $Co(NO_3)_6{\cdot}6H_2O$ was dissolved in 40 mL CH_3OH, denoted as solution A; 10 mmol $C_4H_6N_2$ was dissolved in 40 mL CH_3OH, denoted as solution B. After both solutions turned clear, solution B was rapidly poured into solution A and vigorously stirred for 2 h. Then, centrifugation at 5863 g for 5 min was performed to collect the supernatant.

Preparation of CMF

MF was placed into a tubular furnace, purged with high-purity Ar gas, and heated from room temperature to 800 °C at a rate of 10 °C/min, then maintained for 30 min. After the furnace completely cooled down, CMF was obtained.

Preparation of acidified CC

H_2SO_4 and HNO_3 were mixed in a volume ratio of 3:1 and stirred. After cooling to room temperature, CC was soaked in the mixture for 48 h, then removed, washed repeatedly to remove excess acid, and dried at 60 °C for 24 h.

Preparation of acidified CNTs

A mixture of 200 mL H_2SO_4 and HNO_3 was prepared, and 4 g of dried CNTs was added to the solution. After stirring for 48 h, the mixture was washed to neutral, then dried at 60 °C for 48 h.

The preprocessing of FI

First, cut the FI into small pieces measuring 2 × 2 cm and 1 × 1 cm. Subsequently, immerse the pieces in 0.1 M H_2SO_4 to remove surface oxides. Finally, soak the cleaned FI pieces in 18 M H_2SO_4 to generate a uniform passivation film on the FI surface, preventing oxidation corrosion during use. Rinse thoroughly with deionized water and alcohol, followed by vacuum drying.

Device fabrication

All electrode materials (metal sheet, metal foam, CMF, etc.) were sequentially cleaned in deionized water, alcohol, and acetone for 15 min each, and then dried overnight at 60 °C. The dried CMF was placed in a 25 mL hydrothermal reaction vessel, and a prepared precursor solution of ZIF-67 was added with a loading capacity of 80%, followed by a reaction at 150 °C for 24 h. After cooling to room temperature, the ZIF-67@CMF was removed and washed three times with methanol, dried overnight at 60 °C, and finally combined with FI through pressing to form the electrode material referred to as FI/ZIF67@CMF.

Finite element analysis

Fluid flow movement was simulated using the creeping flow unit and Brinkman equation unit, with a fluid density of 1000 kg/m^3, fluid viscosity of 0.002 kg/(m·s), and a pressure drop of 0.715 Pa.

First-principles calculations

The wave function cutoff energy was set to 400 eV, energy convergence to 10^{-6} eV, and Brillouin zone integration was calculated using a 2 × 2 × 1 mesh for density of states. To prevent interactions between unit cells, a 15 Å surface layer was set. The Castep unit was used to calculate the density of states and differential charge density of material surfaces under different conditions, while the Forcite unit was utilized to compute the molecular dynamics of material surfaces.

Measurements and characterizations

Observation of sample surface morphology and elemental distribution was conducted using a field emission scanning electron microscope (FESEM, Zeiss, Supra55) equipped with an energy dispersive spectrometer. The sample's lattice type was analyzed using an X-ray diffractometer (XRD, Rigaku, Dmax/2500PC). Surface roughness of the sample was observed using a Laser scanning confocal microscope (LSCM, Zeiss, Imager.Z2m). The current density and open-circuit voltage variations of the sample were detected using a digital source meter (DSM, Keithley, 2400). Sample C-V curves were tested using an electrochemical workstation (EW, Corrtest, CS310M). A constant temperature and humidity chamber (THC, Rongsheng, RS/HWHS-216L) provided a stable external environment for sample testing. Obtain Xray photoelectron spectroscopy (XPS) results on the Escalab Xi+ device. The BET results on the ASAP-2020 Plus. The optical microscope (OM) image was captured using a 4XC inverted metallurgical microscope from Shanghai Changfang Optical Instrument Co., Ltd.

Statistics and reproducibility

All test results were randomly obtained from 20 repeated independent experiments.

Reporting summary

Further information on research design is available in the Nature Portfolio Reporting Summary linked to this article.

Data availability

Source data are provided with this paper.

References

1. Gao, X. et al. Electric power generation using paper materials. *J. Mater. Chem. A* **7**, 20574–20578 (2019).
2. Shao, B. et al. Electricity generation from phase transitions between liquid and gaseous water. *Adv. Energy Mater.* **13**, 2204091 (2023).
3. Tan, J., Duan, J., Zhao, Y., He, B. & Tang, Q. Generators to harvest ocean wave energy through electrokinetic principle. *Nano Energy* **48**, 128–133 (2018).
4. Yin, J. et al. Generating electricity by moving a droplet of ionic liquid along graphene. *Nat. Nanotechnol.* **9**, 378–383 (2014).
5. Xu, N. et al. Synergistic tandem solar electricity-water generators. *Joule* **4**, 347–358 (2020).
6. Li, L. et al. A novel, flexible dual-mode power generator adapted for wide dynamic range of the aqueous salinity. *Nano Energy* **85**, 105970 (2021).
7. Fan, K. et al. Spontaneous power generation from broad-humidity atmospheres through heterostructured F/O-bonded graphene monoliths. *Nano Energy* **91**, 106605 (2022).
8. Bai, J. et al. Sunlight-coordinated high-performance moisture power in natural conditions. *Adv. Mater.* **34**, 2103897 (2022).
9. Sun, Z. et al. Electrospun nanofiber fabric: an efficient, breathable and wearable moist-electric generator. *J. Mater. Chem. A* **9**, 7085–7093 (2021).
10. Huang, Y. et al. Interface-mediated hygroelectric generator with an output voltage approaching 1.5 volts. *Nat. Commun.* **9**, 4166 (2018).
11. Shen, D. et al. Self-powered wearable electronics based on moisture enabled electricity generation. *Adv. Mater.* **30**, 1705925 (2018).
12. Wu, Y. et al. A hygroscopic janus heterojunction for continuous moisture-triggered electricity generators. *ACS Appl. Mater. Interfaces* **14**, 19569–19578 (2022).
13. Sohn, S.-H., Choi, G.-J., On, B.-D. & Park, I.-K. Synergistic coupling of tribovoltaic and moisture-enabled electricity generation in layered-double hydroxides. *Adv. Energy Mater.* **14**, 2304206 (2024).
14. Liu, J. et al. Self-regulating and asymmetric evaporator for efficient solar water-electricity generation. *Nano Energy* **86**, 106112 (2021).
15. Li, S.-M. et al. Synergistic effects of TiO_2 and carbon black for water evaporation-induced electricity generation. *ACS Appl. Mater. Interfaces* **16**, 24863–24870 (2024).
16. Xue, W. et al. Power generation from the interaction of a carbon foam and water. *ACS Appl. Mater. Interfaces* **16**, 2825–2835 (2024).
17. Liang, Y. et al. Electric power generation via asymmetric moisturizing of graphene oxide for flexible, printable and portable electronics. *Energy Environ. Sci.* **11**, 1730–1735 (2018).
18. Zhang, Z. et al. Emerging hydrovoltaic technology. *Nat. Nanotechnol.* **13**, 1109–1119 (2018).
19. Fu, C. et al. A long life moisture-enabled electric generator based on ionic diode rectification and electrode chemistry regulation. *Adv. Sci.* **11**, 2305530 (2024).
20. Wang, Z. et al. Hierarchical oriented metal–organic frameworks assemblies for water-evaporation induced electricity generation. *Adv. Funct. Mater.* **31**, 2104732 (2021).
21. Zhang, Z., Liu, C. & Fan, S. Power generation by thermal evaporation based on a button supercapacitor. *ACS Appl. Mater. Interfaces* **16**, 9980–9988 (2024).
22. Hou, B. F. et al. Flexible and portable graphene on carbon cloth as a power generator for electricity generation. *Carbon* **140**, 488–493 (2018).
23. Lin, J. et al. All wood-based water evaporation-induced electricity generator. *Adv.Funct. Mater.* https://doi.org/10.1002/adfm.202314231 (2024).
24. Piao, X. et al. Water-evaporation induced electricity generation inspired by natural tree transpiration. *Sustain. Mater. Technol.* **39**, e00836 (2024).
25. Li, J. et al. Surface functional modification boosts the output of an evaporation-driven water flow nanogenerator. *Nano Energy* **58**, 797–802 (2019).
26. Xue, G. et al. Water-evaporation-induced electricity with nanostructured carbon materials. *Nat. Nanotechnol.* **12**, 317–321 (2017).
27. Kaneti, Y. V. et al. Nanoarchitectured design of porous materials and nanocomposites from metal-organic frameworks. *Adv. Mater.* **29**, 1604898 (2017).
28. Xu, Y. et al. Harvesting solar energy with a Ni-MOF-based evaporator for efficient solar thermal storage and steam generation. *J. Mater. Chem. A* **12**, 12064–12076 (2024).
29. Lin, W.-H. et al. Novel ultrastable 2D MOF/MXene nanofluidic membrane with ultralow resistance for highly efficient osmotic power harvesting. *Nano Energy* **128**, 109924 (2024).
30. Liu, H. et al. Harnessing natural evaporation for electricity generation using MOF-based nanochannels. *Small* **20**, 2400961 (2024).
31. Eun, J. & Jeon, S. Performance enhancement of moisture-driven power generators by photofragmentation of inorganic salt particles. *ACS Appl. Mater. Interfaces* **14**, 45289–45295 (2022).
32. Mo, J. L. et al. Sulfated cellulose nanofibrils-based hydrogel moist-electric generator for energy harvesting. *Chem. Eng. J.* https://doi.org/10.1016/j.cej.2024.152055 (2024).
33. Yang, S. et al. Green moisture-electric generator based on supramolecular hydrogel with tens of milliamp electricity toward practical applications. *Nat. Commun.* **15**, 3329 (2024).
34. Liu, Y. et al. Surface functional modification for boosting power density of hydrovoltaic devices. *Adv. Funct. Mater.* **34**, 2312666 (2024).
35. Liu, X. et al. Microbial biofilms for electricity generation from water evaporation and power to wearables. *Nat. Commun.* **13**, 4369 (2022).
36. Niu, R. et al. Bio-inspired sandwich-structured all-day-round solar evaporator for synergistic clean water and electricity generation. *Adv. Energy Mater.* **13**, 2302451 (2023).
37. Tabrizizadeh, T., She, Z., Stamplecoskie, K. & Liu, G. Empowerment of water-evaporation-induced electric generators via the use of metal electrodes. *ACS Omega* **7**, 28275–28283 (2022).
38. Yu, F. et al. High hydrovoltaic power density achieved by universal evaporating potential devices. *Adv. Sci.* **10**, 2302941 (2023).
39. Wang, X. et al. Carbon cloth functionalized with carbon nanotubes for hydroelectric power generation. *ACS Appl. Nano Mater.* **7**, 7327–7336 (2024).
40. Xing, M. et al. Asymmetrical electrode modified by metal oxide nanoparticles for power generation devices from water evaporation. *Ionics* https://doi.org/10.1007/s11581-024-05529-x (2024).
41. Zhao, F., Cheng, H., Zhang, Z., Jiang, L. & Qu, L. Direct power generation from a graphene oxide film under moisture. *Adv. Mater.* **27**, 4351–4357 (2015).
42. Wang, H. et al. Transparent, self-healing, arbitrary tailorable moist-electric film generator. *Nano Energy* **67**, 104238 (2020).
43. Zhong, G., Liu, D. & Zhang, J. The application of ZIF-67 and its derivatives: adsorption, separation, electrochemistry and catalysts. *J. Mater. Chem. A* **6**, 1887–1899 (2018).
44. Li, B. et al. String of pyrolyzed ZIF-67 particles on carbon fibers for high-performance electrocatalysis. *Energy Storage Mater.* **25**, 137–144 (2020).
45. Sun, X. et al. ZIF-67@Cellulose nanofiber hybrid membrane with controlled porosity for use as Li-ion battery separator. *J. Energy Chem.* **52**, 170–180 (2021).

46. Li, S. & Hihara, L. H. The comparison of the corrosion of ultrapure iron and low-carbon steel under NaCl-electrolyte droplets. *Corros. Sci.* **108**, 200–204 (2016).
47. Alkire, R. C. & Perusich, S. The effect of focused ultrasound on the electrochemical passivity of iron in sulfuric acid. *Corros. Sci.* **23**, 1121–1132 (1983).
48. Zhang, J., Zhang, T., Yu, D., Xiao, K. & Hong, Y. Transition from ZIF-L-Co to ZIF-67: a new insight into the structural evolution of zeolitic imidazolate frameworks (ZIFs) in aqueous systems. *CrystEngComm* **17**, 8212–8215 (2015).
49. Ge, C. et al. Silk fibroin-regulated nanochannels for flexible hydrovoltaic ion sensing. *Adv. Mater.* **36**, 2310260 (2024).
50. Lee, P.-Y. & Lin, L.-Y. Developing zeolitic imidazolate frameworks 67-derived fluorides using 2-methylimidazole and ammonia fluoride for energy storage and electrocatalysis. *Energy* **239**, 122129 (2022).
51. Auset, M. & Keller, A. A. Pore-scale processes that control dispersion of colloids in saturated porous media. *Water Resour. Res.* https://doi.org/10.1029/2003WR002800 (2004).
52. Sirivithayapakorn, S. & Keller, A. Transport of colloids in saturated porous media: a pore-scale observation of the size exclusion effect and colloid acceleration. *Water Resour. Res.* https://doi.org/10.1029/2002WR001583 (2003).
53. Li, X. et al. A hierarchical porous aerohydrogel for enhanced water evaporation. *Water Res.* **244**, 120447 (2023).
54. Wu, D. et al. Self-floating nanostructured Ni–NiOx/Ni foam for solar thermal water evaporation. *J. Mater. Chem. A* **7**, 8485–8490 (2019).
55. Xia, H. et al. Electricity generated by upstream proton diffusion in two-dimensional nanochannels. *Nat. Nanotechnol.* **19**, 1316–1322 (2024).
56. Ghafurian, M. M. et al. Enhanced solar desalination by delignified wood coated with bimetallic Fe/Pd nanoparticles. *Desalination* **493**, 114657 (2020).
57. Zheng, J., Wang, W., Yu, D. & Wang, W. Carbon nanotubes@polydopamine/nickel foam with a wavy shape applied for efficient solar-driven seawater desalination. *Desalination* **567**, 116961 (2023).
58. Li, R. et al. A single component, single layer flexile foam evaporator with the higher efficiency for water generation. *Adv. Mater. n/a* **29**, 2402016 (2024).

Acknowledgements

This research was supported by grants from the National Natural Science Foundation of China (No. 62121005, 62074147, 62474024) Youth Innovation Promotion Association of Chinese Academy of Sciences (2023223) and the Youth Talent Promotion Project of the Chinese Institute of Electronics (No. 2020QNRC001).

Author contributions

Y.Z., L.W., and X.Y. wrote the manuscript. Y.Z. designed and performed all data analyses. F.Y. and Y.J. performed the mathematical calculations for the interaction model. Y.Y., Y.G., and X.L. contributed to data interpretation and result discussion. K.J., W.L., X.S., and D.L. provided funding and resources for the study. X.L., W.L., X.S., and D.L. supervised the study, and all authors contributed to the manuscript.

Competing interests

The authors declare no competing interests.

Additional information

Supplementary information The online version contains supplementary material available at https://doi.org/10.1038/s41467-025-64644-z.

Correspondence and requests for materials should be addressed to Xuesong Li, Wei Lü, Xiaojuan Sun or Dabing Li.

Peer review information *Nature Communications* thanks Yong-Ho Choa, Shien-Ping Feng, and the other, anonymous, reviewer(s) for their contribution to the peer review of this work. A peer review file is available.

Reprints and permissions information is available at http://www.nature.com/reprints